On the direct synthesis of Cu(BDC) MOF nanosheets and their performance in mixed matrix membranes

Meera Shete[a], Prashant Kumar[a], Jonathan E. Bachman[b], Xiaoli Ma[a], Zachary P. Smith[c], Wenqian Xu[d], K. Andre Mkhoyan[a], Jeffrey R. Long[b,e,f], Michael Tsapatsis[a,*]

[a] Department of Chemical Engineering and Materials Science, University of Minnesota, Minneapolis, MN, United States
[b] Department of Chemical and Biomolecular Engineering, University of California, Berkeley, CA, United States
[c] Department of Chemical Engineering, Massachusetts Institute of Technology, Cambridge, MA, United States
[d] X-Ray Science Division, Advanced Photon Source, Argonne National Laboratory, Lemont, IL, United States
[e] Department of Chemistry, University of California, Berkeley, CA, United States
[f] Materials Sciences Division, Lawrence Berkeley National Laboratory, Berkeley, CA, United States

ARTICLE INFO

ABSTRACT

High aspect-ratio nanosheets of metal-organic frameworks (MOFs) hold promise for use as selective flakes in gas separation membranes. However, simple and scalable methods for the synthesis of MOF nanosheets have thus far remained elusive. Here, we describe the direct synthesis of Cu(BDC) (BDC^{2-} = 1,4-benzenedicarboxylate) nanosheets with an average lateral size of 2.5 μm and a thickness of 25 nm from a well-mixed solution. Characterization of the nanosheets by powder and thin film X-ray diffraction, electron microscopy, and electron diffraction reveals pronounced structural disorder that may affect their pore structure. Incorporation of the Cu(BDC) nanosheets into a Matrimid polymer matrix results in mixed matrix membranes (MMMs) that exhibit a 70% increase in the CO_2/CH_4 selectivity compared with that of Matrimid. Analysis of new and previously reported permeation data for Cu(BDC) MMMs using a mathematical model for selective flake composites indicates that further performance improvements could be achieved with the selection of different polymers for use in the continuous phase.

1. Introduction

Metal-organic frameworks (MOFs) are a class of crystalline porous materials with a wide range of pore sizes and functionalities that render them attractive for a variety of potential applications [1,2], including catalysis [3,4], gas storage [5,6], and separations [7–9]. Particularly, certain MOF-based membranes are considered for separation of carbon dioxide from natural gas and flue gas streams [10,11].

Recently, membranes based on zeolite nanosheets were reported to exhibit unprecedented separation performance (high flux and selectivity) [12,13], which motivated the synthesis of MOF nanosheets and exploration of their uses in membrane applications [14–17]. As with other molecular sieve membranes [18], MOF nanosheet-based membranes are typically prepared either by (i) forming intergrown deposits of MOF nanosheets on porous supports in an effort to obtain the intrinsic separation properties of the nanosheets [14,17], or (ii) incorporating the nanosheets in polymer matrices to form mixed matrix membranes (MMMs) [15] that surpass the Robeson upper bound for polymeric membrane performance [19]. It has been convincingly

argued that, from a manufacturing standpoint, the MMM approach is advantageous because it can be readily integrated with existing technologies for forming polymeric membranes [20–22]. Moreover, nanosheet-based MMMs can in principle achieve similar improvements in performance at lower loadings compared to MMMs formed with isotropic crystals [23–26].

The strategies employed for the synthesis of MOF nanosheets can be categorized into: (i) a top-down approach involving exfoliation of layered precursors using techniques such as sonication and ball-milling [14,27], or (ii) a bottom-up approach where crystal growth of MOFs having a tendency to grow anisotropically is tuned to favor the formation of plate-like morphologies by restricting growth along the preferred thin direction either via the adsorption of surfactant-like molecules [16] or by altering the manner in which metal and linker ions come into contact with each other [15]. As recently demonstrated for zeolite nanosheets, the bottom-up approach can often be more advantageous, not only because of its simplicity and higher yields, but also in terms of improved nanosheet quality enabling significantly better membrane performance [28].

Building on an earlier report that required nanosheet crystallization in a three-layer (linker-solvent-metal) gradient [15], we report here the bottom-up synthesis of Cu(BDC) nanosheets by direct homogeneous mixing of the metal and linker solutions. We find that it is possible to tune the aspect-ratio of the nanosheets by varying the synthesis temperature, and carry out detailed structural characterization using electron microscopy and X-ray diffraction. Mixed matrix membranes are successfully fabricated by incorporating the nanosheets into a polymer matrix. We obtain effective permeabilities for the Cu(BDC) nanosheets from permeation data and analyze the MMM performance using a mathematical model.

2. Experimental

2.1. Chemicals

Anhydrous *N,N*-dimethylformamide (DMF, 99%), terephthalic acid (H_2BDC, 98%) and copper nitrate trihydrate ($Cu(NO_3)_2$, 99%) were obtained from Sigma Aldrich. Acetonitrile (CH_3CN, 99.9%), and chloroform ($CHCl_3$, 99.9%) were obtained from Fisher Scientific. Matrimid 5218 was provided by Huntsman Advanced Materials and was degassed at 180 °C under reduced pressure (0.1 bar) for 16–18 h. Chloroform was filtered using a 0.2 μm PTFE syringe filter (Pall Corporation). All other chemicals were used as received.

2.2. Direct synthesis of Cu(BDC) nanosheets

2.2.1. Direct synthesis – no mixing

The metal solution was prepared in a glass vial by adding 1 mL of DMF and 3 mL of CH_3CN to 30 mg of $Cu(NO_3)_2$. The linker solution was prepared by adding 3 mL of DMF and 1 mL of CH_3CN to 30 mg of H_2BDC. The metal solution was added in one portion to the linker solution and the resulting mixture was left to stand at ambient temperature. After 24 h, the solution was centrifuged to obtain Cu(BDC) nanosheets that were then washed 3× in DMF. The nanosheets were stored by suspending them in DMF.

2.2.2. Direct synthesis – gentle mixing with shaker

Typically, the metal solution was prepared in a conical flask by adding 30 mL of DMF and 90 mL of CH_3CN to 900 mg of $Cu(NO_3)_2$ while linker solution was prepared by adding 90 mL of DMF and 30 mL of CH_3CN to 900 mg of H_2BDC. The metal solution was then added dropwise to the linker solution over a period of 40 min under magnetic stirring. After complete addition, the resulting solution mixture was shaken in an orbital shaker (Thermo Scientific MAXQ 4000) at a speed of 200 rpm under a constant temperature (15 °C, 25 °C, or 40 °C). After 24 h at the set temperature, the solution was centrifuged to obtain Cu(BDC) nanosheets, which were then washed 3× in DMF. A suspension of the Cu(BDC) nanosheets in DMF was then solvent exchanged in chloroform by repeated centrifugation. The supernatant was discarded each time and ∼ 40 mL of fresh chloroform was added to the sediment (corresponding to ∼ 2.5 mg of wet nanosheet cake per mL of chloroform). The cake was dispersed by vortexing (Fisher Scientific vortex mixer) for ∼ 5 min, sonicated (Branson 5510R-DTH ultrasonic cleaner) for ∼ 15 min, and then centrifuged. This process was repeated 3×. The nanosheets thus suspended in chloroform were eventually used for the fabrication of MMMs.

2.3. Characterization of Cu(BDC) nanosheets

2.3.1. X-ray diffraction (XRD)

After washing in DMF, the cake of Cu(BDC) nanosheets was oven dried at 70 °C. The dried as-synthesized powder was then added to a polyimide capillary (Cole-Parmer, 0.0395 in. inner diameter × 0.0435 in. outer diameter, 0.6 in. in length) that was then sealed at both ends. X-ray diffraction measurements were performed at beamline 17-

BM at the Advanced Photon Source, Argonne National Laboratory (APS, ANL). A Perkin Elmer amorphous silicon flat panel detector was used to acquire two-dimensional diffraction patterns with program QXRD. The data were converted to traditional xy files of intensity versus 2θ using the GSAS-II program [29]. The X-ray wavelength was 0.24119 Å. Values of 2θ were correspondingly converted to Cu-Kα radiation.

For out-of-plane X-ray diffraction, a suspension of nanosheets in DMF was drop-cast onto a porous silica support [28] to obtain an oriented coating. Out-of-plane X-ray diffraction measurements were performed at Beamline 33-BM-C at APS, ANL using a source wavelength of 0.77493 Å. After converting 2θ values to Cu-Kα radiation, the data were processed using MDI-JADE 2.6.5 software.

Cu(BDC) nanosheets, solvent exchanged in chloroform, were characterized using in-plane X-ray diffraction. The sample was prepared by depositing nanosheets suspended in chloroform onto porous silica supports by vacuum filtration. In-plane measurements were performed at Beamline 33-BM-C at APS, ANL using a source wavelength of 0.77493 Å, and 2θ values were correspondingly converted to Cu-Kα radiation. The data were processed to subtract a linear background using MDI-JADE 2.6.5 software.

2.3.2. Scanning electron microscopy (SEM)

SEM analysis was performed using JEOL 6700 and Hitachi SU8230 scanning electron microscopes. An accelerating voltage of 1.5 kV was used with the JEOL 6700 equipped with a field emission gun. The Hitachi SU8230 was operated in the deceleration mode at a landing voltage of 0.8 kV. Samples for SEM analysis were prepared by drop casting the nanosheet suspension onto a Si wafer.

2.3.3. Transmission electron microscopy (TEM) and selected area electron diffraction (SAED)

A FEI-Tecnai T12 TEM with LaB_6 filament gun operating at 120 kV and equipped with a Gatan MSC794 CCD camera was used for TEM imaging and SAED. Cu(BDC) nanosheets were transferred from suspensions onto lacey carbon films supported on 400 mesh copper grids, and the solvent was allowed to evaporate before TEM analysis. Simulated electron diffraction patterns were obtained using the Single Crystal 2.3 software. Radial averaging of electron diffraction pattern was performed using a MATLAB code to determine the center of the ED pattern, followed by radial averaging of the peak intensity in reciprocal space. A line scan (*counts vs 2θ* after exponential background subtraction), starting from the center of the radially averaged ED pattern, was plotted for comparison with the X-ray diffraction pattern.

2.3.4. Atomic force microscopy (AFM)

A Bruker Nanoscope V Multimode Scanning Probe Microscope was used in tapping mode in the repulsive regime for collecting AFM images. A silicon nitride tip was used, and AFM images were collected at a scan rate of 0.8 Hz and 512 lines/scan. Samples for AFM analysis were prepared by drop casting the nanosheets suspension on a Si wafer. Gwyddion 2.4 software was used to analyze AFM images.

2.3.5. Annular dark-field scanning transmission electron microscopy (ADF-STEM)

Samples for ADF-STEM characterization were prepared by drop-casting a suspension of Cu(BDC) nanosheets onto an ultrathin carbon film on holey carbon support film (400 mesh Cu, from Ted Pella) and allowing the sample to air dry at room temperature. ADF-STEM images were acquired using aberration-corrected FEI Titan 60–300 (S)TEM, equipped with SuperX EDX detector, operating at 60 kV, with a 214 mrad electron probe convergence angle and 30 mrad ADF detector inner angle. The acquired ADF-STEM image was filtered by selecting the spots in Fast Fourier Transform (FFT) of the original image, followed by inverse FFT operation to generate a real space image.

2.4. Fabrication of MMMs

Nanosheets suspended in chloroform were used for fabricating MMMs. To determine the concentration of the stock suspension a *calibration film* was made. A known volume (2 mL) of the suspension in chloroform was added to a 2 wt% solution of Matrimid in chloroform. The MOF-polymer solution was shaken in an orbital shaker at 250 rpm for 1 h and then sonicated for 30 min (Branson 5510R-DTH ultrasonic cleaner). Shaking and sonication cycles were repeated 3× and then the solution was cast in a home-built flat bottom glass well. The solvent was then allowed to evaporate over a period of 24 h, after which time the film was peeled off. The film was activated at 180 °C under reduced pressure (0.1 bar) for 16–18 h. Loading of MOF nanosheets in the *calibration film* was determined by thermogravimetric analysis (TGA) using the data from TGA of MOF nanosheets powder as a reference. TGA was performed using a Shimadzu TGA-50 analyzer. Samples were activated under air (60 mL/min) at 120 °C for 1 h before TGA profiles were collected at a ramp rate of 10 °C/min up to 850 °C. The percentage of mass remaining after ramping to 850 °C was attributed to the mass of metal oxide. By comparing this mass with the mass of metal oxide remaining after TGA on a known weight of MOF powder, the loading of MOF nanosheets in the *calibration film* was determined, and thereby the concentration of the stock solution.

MMMs comprised of different loadings of MOF nanosheets were fabricated following the same procedure as that for the *calibration film*. Film thicknesses were measured using a digital micrometer (Mitutoyo) and found to be in the range of 35–50 μm.

2.5. Single gas permeation measurements

Permeation measurements were performed in a constant-volume, variable-pressure apparatus that was built in-house. A 2.2 cm membrane coupon was cut out from the films and affixed to a stainless-steel fender washer using Loctite epoxy. The fender washer was then sealed tightly in a permeation cell. The system was evacuated overnight before gas permeability measurements were initiated. Permeation of N_2, followed by CO_2, was tested at three different feed pressures. The rate of pressure increase observed upon isolation of the permeate side from vacuum was used to determine the gas permeability values. A leak rate of the system (including the membrane cell) was determined by sealing a dense metal disk into the permeation cell and then measuring the pressure increase on the permeate side upon vacuum isolation. The leak rate was subtracted when calculating the gas permeability using Eq. (1),

$$P = \frac{lV}{Ap_f RT}\left[\left(\frac{dp}{dt}\right)_{ss} - \left(\frac{dp}{dt}\right)_{leak}\right]$$

(1)

where l is the film thickness, V is the volume of the chamber into which the gas is allowed to accumulate, A is the area of the film exposed to the gas, p_f is feed pressure, R is universal gas constant, T is the absolute temperature, $(dp/dt)_{ss}$ is the steady state permeation rate and $(dp/dt)_{leak}$ is the leak rate). Permeability values are reported in the units of Barrer. Leak rates correspond to permeabilities smaller than 0.04 Barrer for a 50 μm film.

2.6. Mixed gas permeation measurements

Mixed gas measurements were performed using a constant volume variable pressure apparatus as described in Ref. [9]. Samples for mixed-gas testing were supported on brass shim stock disks using poly-dimethylsiloxane (PDMS) glue. Supported membranes were loaded in a stainless-steel filter holder (Millipore XX4404700). Feed consisting of a gas mixture of 50:50 CO_2 in CH_4 was flowed at a rate > 100× permeation rate to avoid concentration polarization. The gas mixture was allowed to permeate the membrane until a steady-state permeation rate was reached (> 6-time lags) after which the permeate volume was

evacuated and allowed to accumulate under steady state conditions. The permeate volume collected was then expanded into a mass spectrometer (MKS Microvision 2) for composition analysis. The mass fraction of (mass 44)/ [(mass 44) + (mass15)] was used to determine the mixed gas selectivity. For calibrating the mass fraction, standards with 10%, 50% and 90% CO_2 in CH_4 were used.

3. Results

3.1. Synthesis of Cu(BDC) nanosheets

The bottom-up synthesis of Cu(BDC) nanosheets was first reported by Rodenas and coworkers [15], wherein they used a three-layer gradient scheme that involved separating layers of the metal and linker solutions by a spacer solution to achieve diffusion-mediated modulation of crystal growth kinetics. We found this method to be robust and readily reproducible (Fig. S1). However, gradient crystal growth methods are low-yield and arguably difficult to scale up. Therefore, we explored bottom-up synthesis conditions that would eliminate the need for gradient synthesis. Considering that the inherent crystal growth kinetics of Cu(BDC) favor a plate-like morphology [30–32], we hypothesized that it should be possible to tune the thickness of the bulk crystals and form nanosheets by appropriate variation of the metal and linker concentrations during synthesis as well as the synthesis temperature.

Our first attempt was at synthesis involving direct addition of metal solution to linker solution in one portion and letting the resulting mixture remain static for 24 h at room temperature. Typically, the metal solution was prepared by dissolving the metal salt in a 3:1 vol ratio of CH_3CN: DMF while the linker solution was made by dissolving H_2BDC in a 1:3 vol ratio of CH_3CN: DMF, as described in Section 2.2.1. As seen from Fig. S2a, direct synthesis without any mixing of the synthesis solution yields Cu(BDC) nanosheets that have an average lateral size of 3 μm. Considerable aggregate formation is also observed, which may be due to the formation of secondary nucleation sites on already nucleated and growing nanosheets. These results confirm that, in principle, a direct, bottom-up synthesis can lead to the formation of high-aspect ratio MOF nanosheets.

To avoid aggregation and obtain high quality dispersible nanosheets, we hypothesized that it is important to control MOF nucleation by controlling the sequence and rate of addition of metal and linker solutions when forming the synthesis solution. We also decided to investigate the type of mixing used during synthesis, i.e., magnetic stirring versus gentle shaking using a shaker, anticipating that the later would better preserve the growing nanosheets from fragmentation. As seen from Fig. S2b, addition of the metal to the linker solution dropwise under stirring results in well-faceted nanosheets with sharp edges that also exhibit smaller average lateral sizes and less aggregation than the sheets prepared from a standing solution. Moreover, the addition sequence was found to be important. For example, addition of metal to linker solution resulted in nanosheets with larger lateral dimensions (Fig. S3a) than those made by addition of linker to metal solution (Fig. S3b). While the type of mixing used (magnetic stirring versus shaking) did not have a significant effect on the lateral size and quality of the nanosheets, we decided to use mixing using a shaker in our syntheses.

Based on the screening experiments briefly described above, we adopted a direct synthesis scheme (described in Section 2.2.2) where metal solution is added dropwise to the linker solution over several minutes under magnetic stirring and the resulting synthesis solution is then gently shaken in an orbital shaker at the desired temperature and for the required duration (Fig. 1a). Fig. 1b and c show TEM and SEM images of Cu(BDC) nanosheets synthesized at 15 °C using this method. The average sheet thickness was found to be 25 nm by AFM analysis (Fig. 1d). Fig. 2 shows the effect of synthesis temperature on the lateral size (measured along the edge of the nanosheet) and thickness of Cu(BDC) nanosheets. We found that lower temperatures favor thinner and
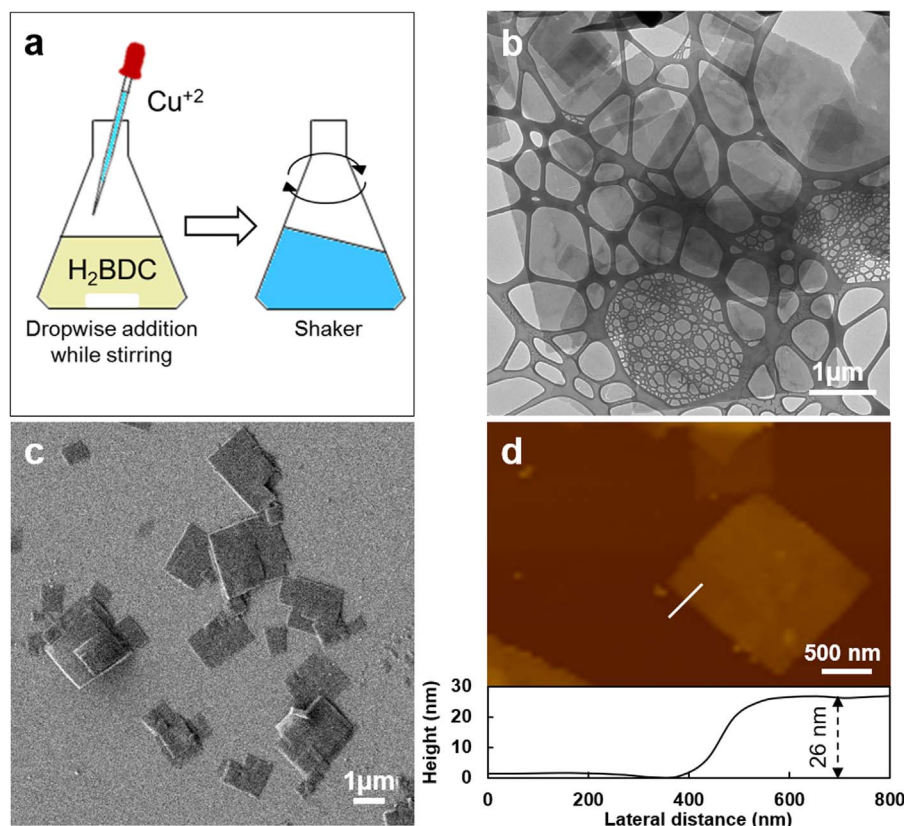
Fig. 1. Direct synthesis of Cu(BDC) nanosheets performed in a shaker at 15 °C for 24 h (synthesis solution was prepared by dropwise addition of Cu^{+2} solution to BDC linker solution under magnetic stirring): (a) Schematic of synthesis procedure, (b) TEM, (c) SEM, and (d) AFM images indicating that the basal dimensions are > 1 µm and the typical thickness is 25 nm.

larger sheets (Fig. 2g and h), and a ten-fold increase in aspect ratio (average lateral dimension/thickness) could be achieved by lowering the synthesis temperature from 40 °C to 15 °C (Fig. 2i). The lateral size distribution of nanosheets synthesized at different temperatures is quantified in Fig. S4, revealing that 85% of the sheets synthesized at 15 °C exhibit lateral sizes between 1–4 µm.

3.2. Structure characterization

Nanosheets obtained from direct synthesis at 15 °C were washed in DMF and the as-synthesized, dried powder was characterized using synchrotron powder X-Ray diffraction. The X-ray diffraction pattern from the as-synthesized nanosheets matches well with the reported structure for solvated Cu(BDC) [33], wherein DMF solvent molecules are coordinated to the metal centers (Fig. 3a).

We further used out-of-plane X-ray diffraction to confirm the crystallographic direction perpendicular to the basal plane of the nanosheets. Samples were prepared by drop casting a suspension of Cu(BDC) nanosheets in DMF onto a porous ceramic support. A comparison of the nanosheet out-of-plane X-ray diffraction pattern (Fig. 3a, red trace) with the nanosheet powder pattern confirms that the solvated nanosheets are oriented in the ($\bar{2}$ 01) direction, as previously reported [15,33]. As seen from the inset in Fig. 3a, the d-spacing for the ($\bar{2}$ 01) peak obtained from the out-of-plane pattern (5.31 Å) is ~ 2% larger than the simulated powder pattern (5.21 Å), whereas the value obtained from the experimental powder pattern (5.18 Å) is very close to the simulated value. This finding indicates that the crystal structure of the Cu(BDC) nanosheets can be affected by processing steps, including attachment to a substrate.

To facilitate incorporation of the Cu(BDC) nanosheets into polymer solutions, the nanosheet suspension in DMF requires exchanging the solvent to chloroform ($CHCl_3$) by repeated centrifugation, and it is therefore important to characterize the nanosheets dispersed in $CHCl_3$. Such characterization has not been previously reported for Cu(BDC)

nanosheets and was performed here using TEM (Fig. 3b and S5). The selected area electron diffraction (SAED) pattern obtained from the nanosheet imaged in Fig. 3b is shown in Fig. 3c. To index the diffraction spots and identify the basal plane orientation, we compared the experimental pattern to simulated electron diffraction patterns for different orientations of the reported structures for Cu(BDC). Qualitatively, a best match was found with the simulated electron diffraction pattern down the a-axis of the reported de-solvated structure [34] (Fig. S6). Thus, the diffraction spots were indexed as (0 k l). Interestingly, a tetragonal projection is evident indicating that the ratio of d-spacings in the b and c directions is near one.

To complement the SAED analysis of solvent-exchanged nanosheets, we also characterized their oriented coating on a porous support using in-plane X-ray diffraction. The in-plane diffraction pattern and the rotationally averaged selected area electron diffraction (RED) pattern are in good agreement with each other and show peaks that mainly correspond to the (0 k l) planes of the de-solvated structure for Cu(BDC) (Fig. S7). Moreover, the in-plane X-ray data are in agreement with the tetragonal projection observed from the electron diffraction pattern, indicating that the length of b and c axes for the Cu(BDC) nanosheets are equal after solvent-exchange in $CHCl_3$. These results point to a structure model (Fig. 3d) with a b-c orientation of the basal plane and pores running down the thin dimension, which is the crystallographic a axis. These pores should be deformed compared to those in the nominal crystal structure [34,35], which indicates differences in b and c axis dimensions.

To confirm that the de-solvated Cu(BDC) exhibits a distorted nearly tetragonal structure, we utilized high-resolution transmission electron microscopy. Indeed, Bragg-filtered ADF-STEM imaging (Fig. 3e) obtained along the direction perpendicular to the nanosheet (a axis) confirms the presence of pores and shows that the planar distances along the b and c directions are almost equal, with a d-spacing of ~1.1 nm. A Bragg filtered ADF-STEM image over a large region of de-solvated Cu(BDC) nanosheet (Fig. S8a) shows the presence of wavy
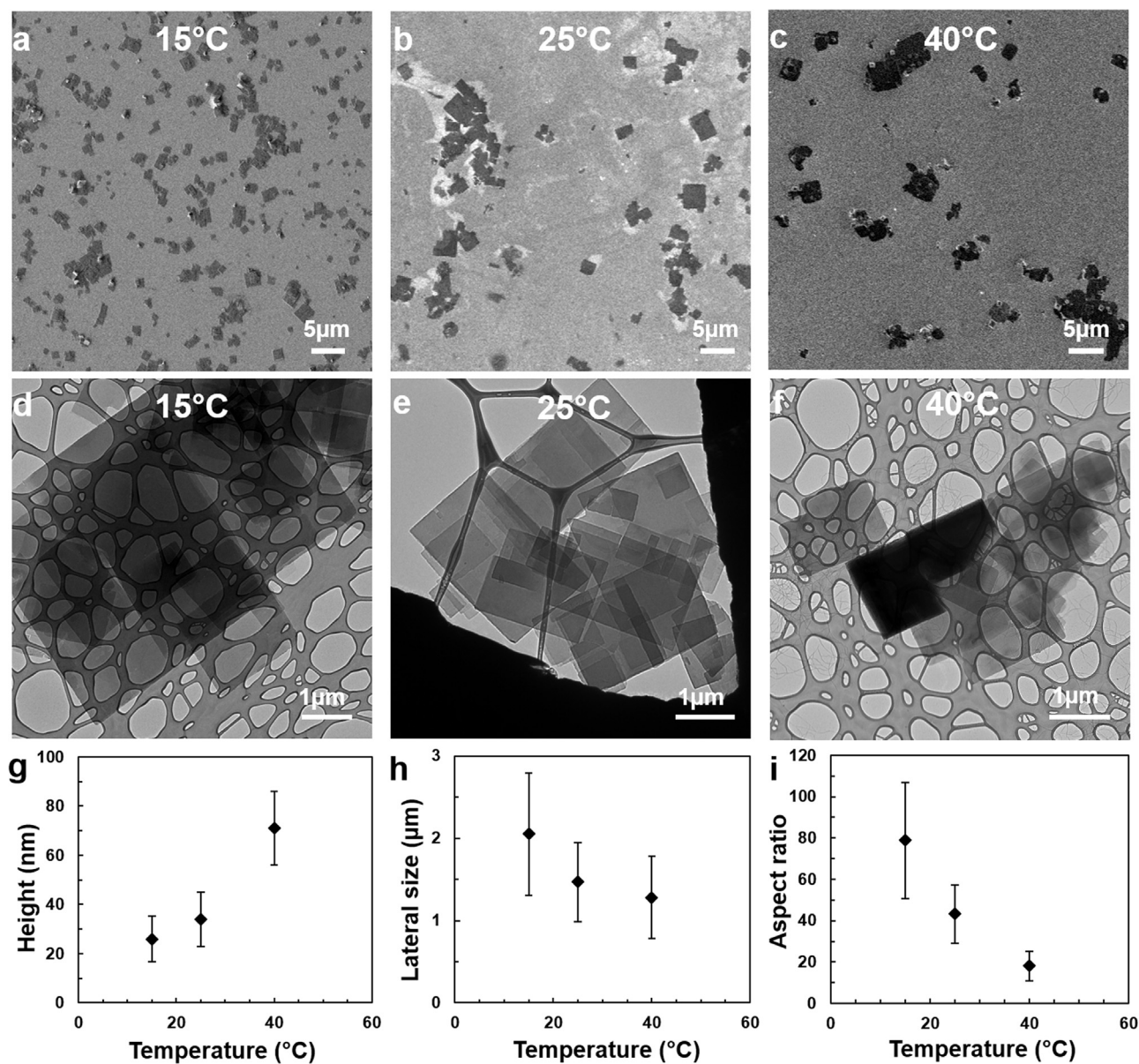
Fig. 2. Effect of temperature on the direct synthesis of Cu(BDC) nanosheets. Low magnification SEM images of nanosheets obtained by direct synthesis at 15 °C, 25 °C and 40 °C are shown in (a), (b), and (c), respectively. TEM images of nanosheets obtained by direct synthesis at 15 °C, 25 °C and 40 °C, are shown in (d), (e), and (f), respectively. Plots of Cu(BDC) nanosheet thickness (g), lateral size (h), and aspect ratio (i) as a function of synthesis temperature.

features along the *b* and *c* axes, which are indicative of structural disorder. Correspondingly, the spots obtained from Fast Fourier Transform (FFT, Fig. S8b) are streaked and so appear to correlate with the peaks exhibiting tails in the in-plane X-ray diffraction pattern (Fig. S7, red trace). The foregoing results confirm a degree of disorder present in the de-solvated structure that has not been identified in earlier studies, and the role of structural disorder in the adsorption and diffusion properties of Cu(BDC) nanosheets is not yet known.

3.3. Membrane performance

Mixed-matrix membranes were fabricated by incorporating Cu(BDC) nanosheets in Matrimid (as detailed in Section 2.4). Nanosheets suspended in chloroform were first mixed with Matrimid to obtain the desired MOF loadings (4, 8, and 12 wt%), and the MMMs were then obtained by solution casting. Single gas (CO_2, N_2) and mixed gas (CO_2/CH_4) measurements were conducted at different feed pressures to test the performance of the MMMs.

At 8 wt% loading of the MOF nanosheets, the ideal selectivity for CO_2/N_2 shows a 70% increase over the pure polymer (Fig. 4a), while the MMM CO_2 and N_2 permeabilities are smaller than those of the neat polymer (Fig. 4b and c). For example, the CO_2 and N_2 permeabilities were observed to decrease by ~ 50% and ~ 70%, respectively, for the 8 wt% MMM relative to the pure polymer at 4 bar (Fig. 4b and c).

The MMMs notably exhibit selectivity for mixed gas feeds at high pressures (Fig. 5a-c). For example, at 12 wt% loading mixed gas measurements show a 70% increase in CO_2/CH_4 selectivity even at 20 bar feed pressure (Fig. 5a). Taken together, these results agree very well with those reported in the literature [15]. Indeed, Rodenas et al. reported a 60% increase for the mixed gas CO_2/CH_4 selectivity at 7.5 bar feed pressure and 8 wt% loading of Cu(BDC) nanosheets in Matrimid. This demonstrates that the directly synthesized Cu(BDC) nanosheets behave similarly with the nanosheets synthesized in Ref. [15], in spite of possible differences due to the structural disorder discussed in Section 3.2. However, we should note two differences between the results presented here and those in Ref. [15]. First, the selectivity for neat
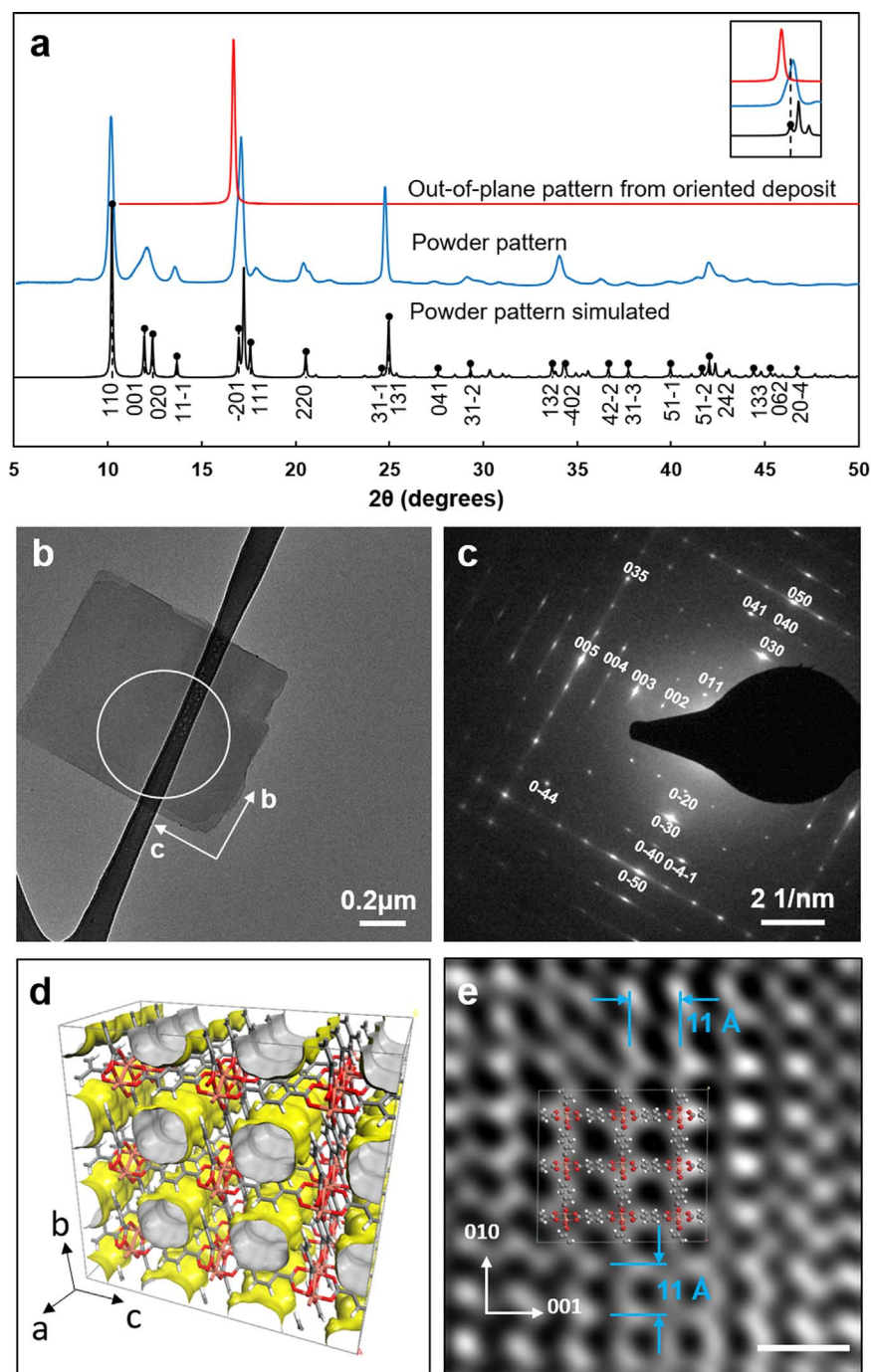
Fig. 3. (a) XRD characterization of as-synthesized (DMF solvated) Cu(BDC) nanosheets; the black trace is the simulated pattern for the reported solvated structure of Cu(BDC) (monoclinic, space group = C2/m; a = 11.41 Å, b = 14.27 Å, c = 7.78 Å, β = 108.12°), the blue trace is the experimental powder pattern, and the red trace is the experimental out-of-plane pattern obtained from oriented Cu(BDC) nanosheets coating on a porous support; the inset shows magnified region for the ($\bar{2}$ 01) peak. (b) TEM image of de-solvated (chloroform washed) Cu(BDC) nanosheets. (c) Selected area electron diffraction pattern obtained from the circled region of nanosheet in (b). (d) Schematic of the Cu(BDC) structure highlighting channels running down the a-axis. (e) Bragg filtered ADF-STEM image of Cu(BDC) nanosheet and superimposition of structure model indicating pores down a-axis. (Scale bar: 2 nm). (For interpretation of the references to color in this figure legend, the reader is referred to the web version of this article.).

Matrimid reported in Ref. [15] is ~ 58, which is much higher than the selectivity value of 24 determined here and more commonly reported for Matrimid in the literature [11,36,37]. These differences could arise due to differences in film fabrication methodology. For example, casting technique, casting solvents, concentration of polymer solution used and film annealing temperature etc. are some of the parameters that can affect the transport properties of polymer films [38]. Second, Rodenas et al. observe an increasing trend in mixed-matrix membrane selectivity as a function of feed pressure, whereas our results show a decreasing trend in selectivity as a function of feed pressure (Fig. 5a).

In a recent study, Yang et al. [39] incorporated Cu(BDC) nanosheets into high permeability polymers such as 6FDA-DAM and PIM-1. They reported a 40% increase in mixed gas CO_2/CH_4 selectivity at 1 bar feed pressure and 4 wt% loading of Cu(BDC) nanosheets in 6FDA-DAM. Considering our permeation results for Matrimid-based MMMs and the

previous reports from Rodenas et al. and Yang et al., we notice that a similar improvement in selectivity is observed by incorporating Cu (BDC) nanosheets in polymers that have CO_2 permeabilities that differ by two orders of magnitude. Given that performance of MMMs depends critically on a good match between the permeability of the polymer matrix and the incorporated nanosheets (selective flake), the following two questions arise. What are the effective permeabilities for Cu(BDC) nanosheets? What are possible polymers that would, in theory, result in a maximum improvement in selectivity?

3.4. Analysis of membrane performance

To address these questions, we resorted to mathematical models that describe transport in MMMs [23,40,41]. The Modified Cussler model [40] is one such model that describes two-dimensional transport
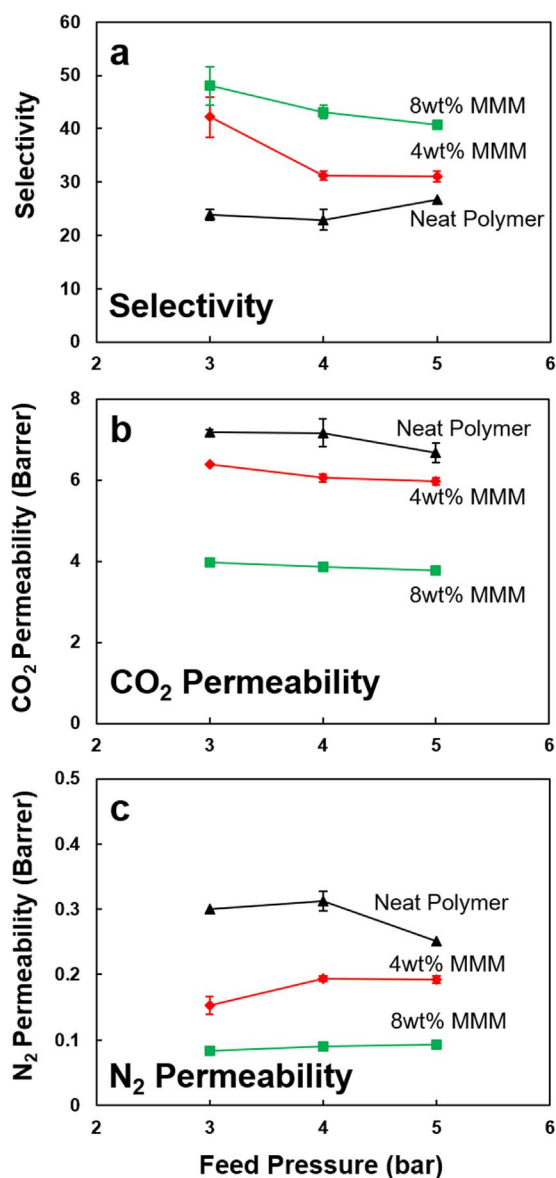
Fig. 4. Single gas CO_2 and N_2 permeation data for Matrimid and mixed matrix membranes incorporating 4 and 8 wt% de-solvated Cu(BDC) nanosheets in Matrimid, showing (a) Ideal selectivity, (b) CO_2 permeability, and (c) N_2 permeability versus feed pressure.
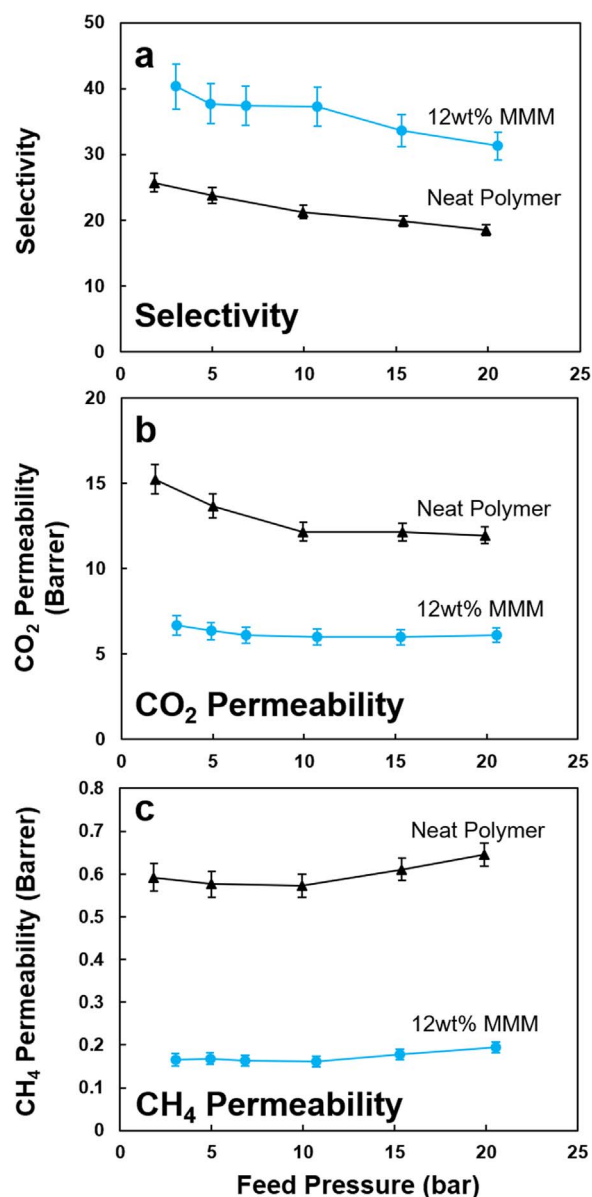

Fig. 5. Mixed gas permeation data from an equimolar CO_2/CH_4 feed for pure Matrimid and a mixed matrix membrane incorporating 12 wt% de-solvated Cu(BDC) nanosheets in Matrimid, showing (a) CO_2/CH_4 Selectivity, (b) CO_2 permeability, and (c) CH_4 permeability versus feed pressure.

across an oriented staggered array of flakes with an aspect ratio, α, dispersed in a polymer matrix at a volume fraction ϕ (Eq. (2)).

$$P_i^C = P_i^M * \frac{1}{(1-\phi) + \frac{1}{\left[\left(\frac{1}{\phi}\right)\left(\frac{P_i^F}{P_i^M}\right) + \left(\frac{1-\phi}{\alpha^2\phi^2}\right)\right]}} \qquad (2)$$

In this equation, P_i^C is the permeability of component i in the mixed matrix membrane (composite); P_i^M is the permeability of component i in polymer matrix; and P_i^F is the permeability of component i in the flake (incorporated nanosheet). The model assumes idealized flakes that are regularly spaced and dispersed uniformly in the continuous polymer matrix. Also, the matrix and flake permeabilities are assumed to be constant (concentration independent). Eq. (2) has been shown to describe well permeation in selective-flake MMMs when the volume fraction is low and the aspect ratio high, as is the case with the MMMs studied here.

Using our permeation results at the 4 and 8 wt% loadings and given an average Cu(BDC) nanosheet aspect ratio of 80, Eq. (1) is used to determine flake permeability for CO_2 and N_2. Flake permeability values

obtained for CO_2 are in the range of 0.7–1.9 Barrer and those for N_2 are in the range of 0.009–0.012 Barrer. It is worth noting that the flake permeabilities calculated here based on the permeation data from the MMMs are effective values and could be influenced by the structure of the MMMs and their fabrication history. As discussed in Section 3.3, effective flake permeability lower than the matrix permeability accounts for the observed reduction in permeability upon incorporation of Cu(BDC) nanosheets in the polymer matrix.

Flake selectivities in the range of 80–160 are estimated from the effective permeability values. Given that the adsorptive selectivity of the thermally de-solvated Cu(BDC) nanosheets for CO_2 over N_2 is in the range of 3–5 [15,34], using Eq. (3),

$$\frac{P_i^F}{P_j^F} = \frac{D_i^F}{D_j^F} \times \frac{S_i^F}{S_j^F} \qquad (3)$$

where D is the diffusivity and S is the solubility, one would obtain a diffusive selectivity value for the Cu(BDC) flakes in the range of 20–50.

Table 1

Comparison of permeation results for 4 wt% Cu(BDC)-based MMMs in the literature. The model predictions were obtained using the modified Cussler equation as described in Section 3.4. Flake permeabilities (PCO_2 = 1.92; PN_2 = 0.012) were determined from MMM (4 wt% Cu(BDC) in Matrimid matrix) permeation results and then used along with the corresponding matrix permeabilities to calculate the model predictions for MMM performance.

	Selectivity			Permeability of CO_2 (Barrer)		
	Neat Polymer	4 wt% Cu(BDC) MMM		Neat Polymer	4 wt% Cu(BDC) MMM	
	Experimental	Experimental	Model Prediction	Experimental	Experimental	Model Prediction
Matrimid (Ref. [15])	58	68	70	5.78	4.74	5.3
Matrimid (This Work)	24	42	42	7.2	6.4	6.4
6FDA-DAM (Ref. [39])	30	43	48	590	430	73.7
PIM-1 (Ref. [39])	17	22	20	3100	2300	241.9

It will be interesting if follow up studies can confirm such high diffusion selectivity for CO_2 over N_2. If indeed the Cu(BDC) nanosheets have the model-estimated permeabilities, then by appropriate selection of a polymer matrix, MMMs with even better performance can be obtained. For example, if the polymer matrix is selected to be 6FDA-DAT with CO_2 and N_2 permeabilities of 56 and 1.12 Barrer, respectively, then a 8 wt% MMM should theoretically exhibit CO_2 and N_2 permeance values of 16.23 and 0.17 Barrer, giving a selectivity of 98. However, as discussed below, it appears that there are inconsistencies with other reported MMM data, indicating that other factors such as the polymer matrix-Cu(BDC) interface may contribute to the observed permeances and selectivities.

We used the flake permeabilities obtained from our permeation data at 4 wt% loading of Cu(BDC) nanosheets in Matrimid to predict the performance of the 4 wt% Cu(BDC) based MMMs reported in Refs. [15,39] (Table 1). The neat polymer selectivity values used for making the predictions are reported in the first column of Table 1. We see that the selectivities predicted from the modified Cussler equation (column three in Table 1) agree very well with the experimental values (column two). Also, the model predictions for CO_2 permeability for Matrimid-based MMMs (Ref. [15] and this work, column six) agree very well with the experimental data (column five). However, the model predictions for CO_2 permeability for 6FDA-DAM and PIM-1 MMMs are much lower than the values reported in Ref. [39]. One possible explanation for the experimental results of Ref. [39] is that incorporation of Cu(BDC) nanosheets in 6FDA-DAM and PIM-1 leads to the formation of non-selective void space around the nanosheets through which the gases can bypass, leading to the measured high permeabilities of CO_2 and CH_4 [42,43]. However, this explanation cannot account for the observed selectivity improvements in the MMMs (43% for 6FDA-DAM MMM and 19% for PIM-1), unless it is accompanied with a modification of the polymer matrix induced by the nanosheets and/or processing conditions.

4. Conclusions

Using direct syntheses carried out at 15 °C, we obtained Cu(BDC) nanosheets with aspect ratios as high as 100 (average lateral size 2.5 μm and thickness of 25 nm). Dropwise addition of the metal to the linker solution under magnetic stirring followed by gentle mixing of the synthesis solution in a shaker resulted in high quality, dispersible nanosheets. It was found that reducing the synthesis temperature from 40 °C to 15 °C results in a ten-fold increase in the aspect ratio of Cu(BDC) nanosheets.

Solvent exchanging of the DMF-soaked sheets with $CHCl_3$ resulted in desolvation, and the de-solvated nanosheets were characterized in detail for the first time using high-resolution TEM imaging and electron and X-ray diffraction. When compared to the nominal crystal structure reported previously, the de-solvated nanosheets show presence of structural disorder.

Incorporation of de-solvated Cu(BDC) nanosheets in Matrimid led to

a maximum 70% increase in the CO_2/CH_4 mixture separation factor at 12 wt% loading and 20 bar pressure for a 50:50 $CO_2:CH_4$ feed. A CO_2 permeability of 6.1 Barrer was observed for the 12 wt% loaded MMM, as compared to a CO_2 permeability of 12 Barrer for Matrimid. Using the experimental permeation results obtained in this work with a mathematical model for transport in mixed matrix membranes, the effective permeabilities of Cu(BDC) nanosheets were estimated and further used to predict the performance of Cu(BDC)-based mixed matrix membranes reported in the literature. Certain of the experimental permeability values reported are much higher than those predicted using the model, indicating the presence of defects at the matrix-flake interface. If one can avoid these defects while fabricating MMMs, a four-fold improvement in the selectivity should be achievable at 8 wt% loading of Cu(BDC) nanosheets in a polymer matrix that has a CO_2 permeability of around 60 Barrer.

Appendix A. Supplementary material

Supplementary data associated with this article can be found in the online version at http://dx.doi.org/10.1016/j.memsci.2017.12.002.

References

[1] O.M. Yaghi, M. O'Keeffe, N.W. Ockwig, H.K. Chae, M. Eddaoudi, Kim Jaheon, Reticular synthesis and the design of new materials, Nature 423 (2003) 705–712.

[2] H. Furukawa, K.E. Cordova, M. O'Keeffe, O.M. Yaghi, The chemistry and applications of metal-organic frameworks, Science 341 (2013) 1230444-1–1230444–12.

[3] J. Lee, O.K. Farha, J. Roberts, K.A. Scheidt, S.T. Nguyen, J.T. Hupp, Metal-organic framework materials as catalysts, Chem. Soc. Rev. 38 (2009) 1450–1459.

[4] P. García-García, M. Müller, A. Corma, MOF catalysis in relation to their homogeneous counterparts and conventional solid catalysts, Chem. Sci. 5 (2014) 2979–3007.

[5] A.R. Millward, O.M. Yaghi, Metal-organic frameworks with exceptionally high capacity for storage of carbon dioxide at room temperature, J. Am. Chem. Soc. 127 (2005) 17998–17999.

[6] L.J. Murray, M. Dincă, J.R. Long, Hydrogen storage in metal–organic frameworks, Chem. Soc. Rev. 38 (2009) 1294.

[7] J.-R. Li, J. Sculley, H. Zhou, Metal-organic frameworks for separations, Chem. Rev. 112 (2012) 869–932.

[8] T.M. McDonald, J.A. Mason, X. Kong, E.D. Bloch, D. Gygi, A. Dani, V. Crocellà, F. Giordanino, S.O. Odoh, W.S. Drisdell, B. Vlaisavljevich, A.L. Dzubak, R. Poloni, S.K. Schnell, N. Planas, K. Lee, T. Pascal, L.F. Wan, D. Prendergast, J.B. Neaton, B. Smit, J.B. Kortright, L. Gagliardi, S. Bordiga, J.A. Reimer, J.R. Long, Cooperative insertion of CO_2 in diamine-appended metal-organic frameworks, Nature 519 (2015) 303–308.

[9] J.E. Bachman, Z.P. Smith, T. Li, T. Xu, J.R. Long, Enhanced ethylene separation and plasticization resistance in polymer membranes incorporating metal–organic framework nanocrystals, Nat. Mater. 15 (2016) 845–849.

[10] B. Seoane, J. Coronas, I. Gascon, M.E. Benavides, O. Karvan, J. Caro, F. Kapteijn, J. Gascon, Metal–organic framework based mixed matrix membranes: a solution for highly efficient CO_2 capture? Chem. Soc. Rev. 44 (2015) 2421–2454.

[11] J.E. Bachman, J.R. Long, Plasticization-resistant Ni 2 (dobdc)/polyimide composite membranes for the removal of CO_2 from natural gas, Energy Environ. Sci. 9 (2016) 2031–2036.

[12] K. Varoon, X. Zhang, B. Elyassi, D.D. Brewer, M. Gettel, S. Kumar, J.A. Lee, S. Maheshwari, A. Mittal, C.-Y. Sung, M. Cococcioni, L.F. Francis, A.V. McCormick, K.A. Mkhoyan, M. Tsapatsis, Dispersible exfoliated zeolite nanosheets and their application as a selective membrane, Science 334 (2011) 72–75.

[13] K.V. Agrawal, B. Topuz, T.C.T. Pham, T.H. Nguyen, N. Sauer, N. Rangnekar, H. Zhang, K. Narasimharao, S.N. Basahel, L.F. Francis, C.W. Macosko, S. Al-Thabaiti, M. Tsapatsis, K.B. Yoon, Oriented MFI membranes by gel-less secondary growth of sub-100 nm MFI-nanosheet seed layers, Adv. Mater. 27 (2015) 3243–3249.

[14] Y. Peng, Y. Li, Y. Ban, H. Jin, W. Jiao, X. Liu, W. Yang, Metal-organic framework nanosheets as building blocks for molecular sieving membranes, Science 346 (2014) 1356–1359.

[15] T. Rodenas, I. Luz, G. Prieto, B. Seoane, H. Miro, A. Corma, F. Kapteijn, F.X. Llabrés i Xamena, J. Gascon, Metal – organic framework nanosheets in polymer composite materials for gas separation, Nat. Mater. 14 (2015) 48–55.

[16] M. Zhao, Y. Wang, Q. Ma, Y. Huang, X. Zhang, J. Ping, Z. Zhang, Q. Lu, Y. Yu, H. Xu, Y. Zhao, H. Zhang, Ultrathin 2D metal-organic framework nanosheets, Adv. Mater. 27 (2015) 7372–7378.

[17] X. Wang, C. Chi, K. Zhang, Y. Qian, K.M. Gupta, Z. Kang, J. Jiang, D. Zhao, Reversed thermo-switchable molecular sieving membranes composed of two-dimensional metal-organic nanosheets for gas separation, Nat. Commun. 8 (2017) 14460.

[18] N. Rangnekar, N. Mittal, B. Elyassi, J. Caro, M. Tsapatsis, Zeolite membranes – a review and comparison with MOFs, Chem. Soc. Rev. 44 (2015) 7128–7154.

[19] L.M. Robeson, The upper bound revisited, J. Membr. Sci. 320 (2008) 390–400.

[20] R. Mahajan, W.J. Koros, Factors controlling successful formation of mixed-matrix gas separation materials, Ind. Eng. Chem. Res. 39 (2000) 2692–2696.

[21] W.J. Koros, R. Mahajan, Pushing the limits on possibilities for large scale gas separation: which strategies? J. Membr. Sci. 175 (2000) 181–196.

[22] M. Galizia, W.S. Chi, Z.P. Smith, T.C. Merkel, R.W. Baker, B.D. Freeman, 50th Anniversary perspective: polymers and mixed matrix membranes for gas and vapor separation: a review and prospective opportunities, Macromolecules (2017).

[23] E.L. Cussler, Membranes containing selective flakes, J. Membr. Sci. 52 (1990) 275–288.

[24] H.-K. Jeong, W. Krych, H. Ramanan, S. Nair, E. Marand, M. Tsapatsis, Fabrication of polymer/selective-flake nanocomposite membranes and their use in gas separation, Chem. Mater. 16 (2004) 3838–3845.

[25] S. Choi, J. Coronas, E. Jordan, W. Oh, S. Nair, F. Onorato, D.F. Shantz, M. Tsapatsis, Layered silicates by swelling of AMH-3 and nanocomposite membranes, Angew. Chem. - Int. Ed. 47 (2008) 552–555.

[26] W. Kim, S. Nair, Membranes from nanoporous 1D and 2D materials: a review of opportunities, developments, and challenges, Chem. Eng. Sci. 104 (2013) 908–924.

[27] P.-Z. Li, Y. Maeda, Q. Xu, Top-down fabrication of crystalline metal–organic framework nanosheets, Chem. Commun. 47 (2011) 8436.

[28] M.Y. Jeon, D. Kim, P. Kumar, P.S. Lee, N. Rangnekar, P. Bai, M. Shete, B. Elyassi, H.S. Lee, K. Narasimharao, S.N. Basahel, S. Al-Thabaiti, W. Xu, H.J. Cho, E.O. Fetisov, R. Thyagarajan, R.F. DeJaco, W. Fan, K.A. Mkhoyan, J.I. Siepmann, M. Tsapatsis, Ultra-selective high-flux membranes from directly synthesized zeolite nanosheets, Nature 543 (2017) 690–694.

[29] B.H. Toby, R.B. Von Dreele, GSAS-II: the genesis of a modern open-source all purpose crystallography software package, J. Appl. Crystallogr. 46 (2013) 544–549.

[30] W. Mori, F. Inoue, K. Yoshida, H. Nakayama, S. Takamizawa, M. Kishita, Synthesis of new adsorbent copper(II) terephthalate, Chem. Lett. (1997) 1219–1220.

[31] Z. Xin, J. Bai, Y. Shen, Y. Pan, Hierarchically micro- and mesoporous coordination polymer nanostructures with high adsorption performance, Cryst. Growth Des. 10 (2010) 2451–2454.

[32] C. Yim, S. Jeon, Direct synthesis of Cu-BDC frameworks on a quartz crystal microresonator and their application to studies of n-hexane adsorption, RSC Adv. 5 (2015) 67454–67458.

[33] C.G. Carson, K. Hardcastle, J. Schwartz, X. Liu, C. Hoffmann, R.A. Gerhardt, R. Tannenbaum, Synthesis and structure characterization of copper terephthalate metal-organic frameworks, Eur. J. Inorg. Chem. (2009) 2338–2343.

[34] C.G. Carson, G. Brunnello, S.G. Lee, S.S. Jang, R.A. Gerhardt, R. Tannenbaum, Structure solution from powder diffraction of copper 1,4- benzenedicarboxylate, Eur. J. Inorg. Chem. (2014) 2140–2145.

[35] K. Seki, S. Takamizawa, W. Mori, Characterization of microporous copper(II) dicarboxylates (fumarate, terephthalate, and trans-1,4-cyclohexanedicarboxylate) by gas adsorption, Chem. Lett. (2001) 122–123.

[36] T.S. Chung, S.S. Chan, R. Wang, Z. Lu, C. He, Characterization of permeability and sorption in Matrimid/C60 mixed matrix membranes, J. Membr. Sci. 211 (2003) 91–99.

[37] Y. Zhang, I.H. Musselman, J.P. Ferraris, K.J. Balkus, Gas permeability properties of Matrimid® membranes containing the metal-organic framework Cu-BPY-HFS, J. Membr. Sci. 313 (2008) 170–181.

[38] P. Hacarlioglu, L. Toppare, L. Yilmaz, Effect of preparation parameters on performance of dense homogeneous polycarbonate gas separation membranes, J. Appl. Polym. Sci. 90 (2003) 776–785.

[39] Y. Yang, K. Goh, R. Wang, T.-H. Bae, High-performance nanocomposite membranes realized by efficient molecular sieving with CuBDC nanosheets, Chem. Commun. 53 (2017) 4254–4257.

[40] J.A. Sheffel, M. Tsapatsis, A model for the performance of microporous mixed matrix membranes with oriented selective flakes, J. Membr. Sci. 295 (2007) 50–70.

[41] J.A. Sheffel, M. Tsapatsis, A semi-empirical approach for predicting the performance of mixed matrix membranes containing selective flakes, J. Membr. Sci. 326 (2009) 595–607.

[42] R. Mahajan, W.J. Koros, Mixed matrix membrane materials with glassy polymers. Part 1, Polym. Eng. Sci. 42 (2002) 1420–1431.

[43] T.T. Moore, W.J. Koros, Non-ideal effects in organic-inorganic materials for gas separation membranes, J. Mol. Struct. 739 (2005) 87–98.